Orbital and magnetic ordering in the weak ferromagnet vanadium trifluoride VF_3

Reinhard K. Kremer [1,*] Florian Kraus [2,†] Patrick Woidy [2] Gwilherm Nénert [3,‡,§]
Christina Drahten,[4,‖,¶] and Bachir Ouladdiaf [3,**]

[1] *Max Planck Institute for Solid State Research, Heisenbergstrasse 1, 70569 Stuttgart, Germany*
[2] *Fachbereich Chemie, Philipps-Universität Marburg, 35032 Marburg, Germany*
[3] *Institut Max von Laue Paul Langevin, 38042 Grenoble, France*
[4] *European Synchrotron Radiation Facility, Grenoble, 38000 Grenoble, France*

(Received 6 November 2025; revised 20 January 2026; accepted 23 January 2026; published 25 February 2026)

We report on an investigation of the low-temperature structural, thermal, and magnetic properties of the binary trifluoride VF_3 by temperature-dependent magnetization, heat capacity, electron paramagnetic resonance, and synchrotron powder and neutron powder diffraction measurements. At room temperature the crystal structure of VF_3 features V^{3+} spin $S = 1$ regular triangular layers. At ∼120 K VF_3 undergoes a structural phase transition, and at ∼18 K it undergoes an antiferromagnetic phase transition. The structural phase transition involves a minute orthorhombic distortion of the regular octahedral fluorine coordination shell of the trivalent V cations, effecting a distortion to the monoclinic crystal system. The magnetic phase transition generates a weak ferromagnet with V magnetic moments essentially confined to the trigonal planes of the room temperature structure described in the space group $R-3c$. The ordered magnetic moments of the V^{3+} cations amount to $\approx 1\mu_B$ and is thus distinctly reduced from the spin-only magnetic moment of $2\mu_B$. This finding and the weak ferromagnetic moment are discussed in view of the low-symmetry structure and spin-orbit effects on the $^3T_1$ cubic ground term of the V^{3+} d^2 system.

DOI: 10.1103/3gzm-yxfb

I. INTRODUCTION

Binary 3*d* transition metal trifluorides MF_3 (M = V, Cr, Fe, Co) crystallize in the trigonal crystal system (space group $R\bar{3}c$; see Fig. 1). Their crystal structure contains triangular M layers connected perpendicularly to [111] to adjacent layers via common F atoms [1–4]. In contrast, already at room temperature MnF_3 exhibits a monoclinic distortion and crystallizes in the space group $C2/c$ (No. 15) [5,6]. MF_3 compounds were among the first systems which were investigated by neutron powder diffraction with respect to their magnetic ordering properties [7]. FeF_3 and CoF_3 are antiferromagnets and exhibit Néel temperatures well above room temperature: 362 and 460 K for FeF_3 and CoF_3, respectively [7,8]. CrF_3 and MnF_3 undergo long-range antiferromagnetic order at significantly lower temperatures, namely, at 75 and 45 K, respectively [9–11]. A small "parasitic" magnetic moment was detected for CrF_3, characterizing CrF_3 as a weak ferromagnet [10]. FeF_3 and CoF_3 show different magnetic structures. Whereas in FeF_3 the magnetic moments of Fe^{3+} cations lie in the plane perpendicular to the threefold axis, the moments in CoF_3 align parallel to the threefold axis [12]. For CoF_3, Lee *et al.* found an additional anomaly at ∼40 K which they discussed in terms of weak ferromagnetism due to an interplay of spin tilting and Dzyaloshinskii-Moriya interactions [12].

Wollan *et al.* also investigated VF_3 by neutron powder diffraction but did not observe any indication of magnetic long-range order down to 4.2 K [7]. However, in 1972 Gossard *et al.* studied the magnetic susceptibility, the heat capacity, and ^{51}V and ^{19}F nuclear magnetic resonance (NMR) of VF_3. They observed magnetic order below 19.4 K and an additional anomaly at 122 K which, based on the NMR results, was ascribed to a structural phase transition (PT) [13]. Similar to CoF_3, the magnetic susceptibility of VF_3 exhibits a weak ferromagnetic moment below ∼19 K. The magnetic susceptibility is affected by the structural PT. The inverse susceptibility changes slope at around 120 K, indicating a reduction of the effective magnetic moment. Gossard *et al.* reported effective magnetic moments of $2.98\mu_B$ and $2.5\mu_B$ above and below the structural PT, respectively. Assuming a spin $S = 1$ ground state for V^{3+}, this finding corresponds to a reduction of the g factor from 2.11 to 1.77 for the high- and low-temperature magnetic properties [13]. Also, the Curie-Weiss temperature is reduced from −112 to −32 K. Interestingly, the magnetic entropy associated with the magnetic PT at ∼19 K amounts to only $0.77R$, where R is the molar gas constant [13]. This value is markedly lower than

*Contact author: R.Kremer@fkf.mpg.de
†Contact author: f.kraus@uni-marburg.de
‡Contact author: gwilherm.nenert@malvernpanalytical.com
§Present address: Malvern Panalytical B.V. Lelyweg 1, 7602 EA Almelo, The Netherlands.
‖Contact author: christina.drahten@thermofisher.com
¶Present address: Thermo Fisher Scientific GmbH, Im Steingrund 4, 63303 Dreieich, Germany.
**Contact author: ouladdia@ill.fr

Published by the American Physical Society under the terms of the Creative Commons Attribution 4.0 International license. Further distribution of this work must maintain attribution to the author(s) and the published article's title, journal citation, and DOI. Open access publication funded by Max Planck Society.

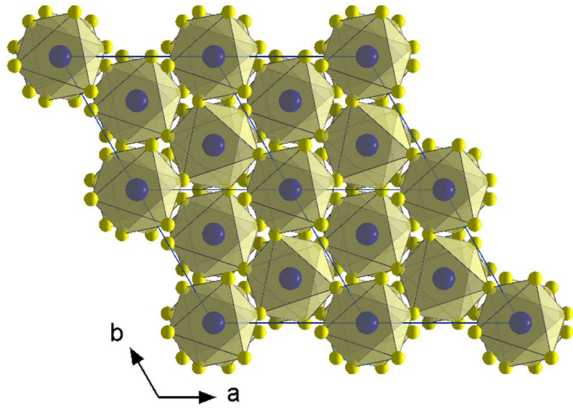


FIG. 1. Room temperature crystal structure of 3*d* transition metal trifluorides MF_3 (M = V, Cr, Fe, Co) projected along the threefold axis. *M* atoms are depicted in blue, F atoms are in yellow, and F octahedral polyhedra are highlighted.

$\ln(2S+1)R = 1.1R$ expected for a spin $S = 1$ system, but rather close to the value $\ln(2R) = 0.69R$ observed for ordering in a twofold degenerate ground state system.

Here, we report on a detailed reinvestigation of the structural and magnetic properties of VF_3. We prepared a large polycrystalline sample and characterized it by magnetic susceptibility, heat capacity, electron paramagnetic resonance (EPR) experiments, synchrotron powder diffraction (SPD), and neutron powder diffraction (NPD). We confirm the structural PT at ∼122 K and determine the low-temperature monoclinic crystal structure. It involves a minute monoclinic distortion of the high-temperature trigonal structure leading to a slight differentiation of the V atom distances to the F atoms in the octahedral coordination shell. The magnetic structure below the antiferromagnetic PT at ∼19 K can be understood as an *A*-type antiferromagnetic structure with the magnetic moments essentially perpendicular to the threefold axis of the high-temperature $R\bar{3}c$ crystal structure, similar to the finding for FeF_3. Canting of the moments leading to weak ferromagnetism, which is evident from the magnetic susceptibility measurements, could not be resolved from the powder diffraction measurements. The ordered magnetic moment is found to be $\sim 1\mu_B$, significantly reduced from that expected for a spin $S = 1$ system with a *g* factor close to 2.

II. EXPERIMENT

A large powder sample of VF_3 was synthesized by reacting black vanadium(III) oxide (V_2O_3; Merck, purity = 99.5%) with HF (Solvay). V_2O_3 was placed in a passivated magnesium boat into a tube furnace. The furnace was purged with Ar gas for 10 min before switching to gaseous HF. The temperature was raised to 400 °C at a rate of 2 K/min and kept at 400 °C for 4 h. Subsequently, the oven was cooled down to 50 °C at a rate of 2 K/min. Finally, HF gas was flushed away with an Ar stream.

Magnetic susceptibilities were measured in a MPMS X7 Squid magnetometer (Quantum Design). The polycrystalline sample was sealed in a fused silica tube filled with ∼1 bar ^{4}He atmosphere to ensure sufficient thermal contact. The heat capacities of a polycrystalline sample immersed in Apiezon N vacuum grease were measured using the relaxation method installed in a physical properties measurement system (Quantum Design). The heat capacities of the vacuum grease and the sapphire sample platform were determined in a preceding run and subtracted from the measured total heat capacities. EPR spectra were acquired for a powder sample between 4 K and room temperature using a Bruker ER040XK microwave *X*-band (9.48 GHz) spectrometer equipped with a Bruker BE25 and a BH15 field controller calibrated against 1,1-diphenyl-2-picryl-hydrazyl (DPPH).

NPD patterns were collected between 1.65 and 22 K with the high-intensity two-axis diffractometer D20 installed at the Institut Laue-Langevin (ILL). The neutron wavelength was set to 2.42 Å [14]. The powder sample was placed into an 8 mm outer diameter thin-walled vanadium can under ∼1 bar ^{4}He exchange gas to ensure rapid thermal equilibration. SPD patterns were collected using the European Synchrotron Radiation Facility's (ESRF) high-energy beamline ID 31. The sample was contained in an ∼0.3 mm outer diameter fused silica capillary also filled with 1 bar ^{4}He gas. For temperatures above ∼80 K a nitrogen stream cooler was employed to set the temperature of the sample. The synchrotron radiation wavelength was determined using a Si standard sample, and it amounted to 0.3542 Å. For temperatures below 22 K a He cryostat was used (λ = 0.3996 Å). Profile Rietveld refinements of the SPD and NPD patterns were performed using the fullprof software suite [15]

III. RESULTS AND DISCUSSION

A. Magnetic and thermal properties

Figure 2 displays the magnetic susceptibility data of our VF_3 polycrystalline sample measured in external magnetic fields of 1 and 10 kOe. Above ∼200 K the inverse magnetic susceptibilities follow a Curie-Weiss law according to

$$\chi_{CW} = \frac{N_A \mu_B^2 p_{eff}^2}{3k_B(T-\theta)} + \chi_0. \quad (1)$$

N_A and k_B are the Avogadro and Boltzmann constants, respectively. θ is the Curie-Weiss temperature, and χ_0 accounts for a temperature-independent contribution to the susceptibility resulting from the diamagnetic susceptibility of the electrons in the closed electron shells. χ_0 was calculated from Pascal's increments tabulated, e.g., by Bain and Berry to be -37.5×10^{-6} cm^3/mol [16]. The effective magnetic moment p_{eff} is defined as

$$p_{eff} = g\sqrt{S(S+1)}, \quad (2)$$

with *g* being the *g* factor and *S* being the spin value.

A fit of the high-temperature ($T > 200$ K) susceptibility data with Eq. (1) yields an effective magnetic moment of $p_{eff} = 2.99(1)\mu_B$ and a Curie-Weiss temperature $\theta = -127(1)$ K, in good agreement with results found previously [13]. With Eq. (2) the effective moment corresponds to a *g* factor of 2.12(1).

Below ∼120 K the inverse susceptibility changes slope, indicating a reduction of the effective moment. A fit of the inverse susceptibilities between 35 and 100 K to Eq. (1) yields an effective moment and a Curie-Weiss temperature of

$$p_{eff} = 2.4(1)$$

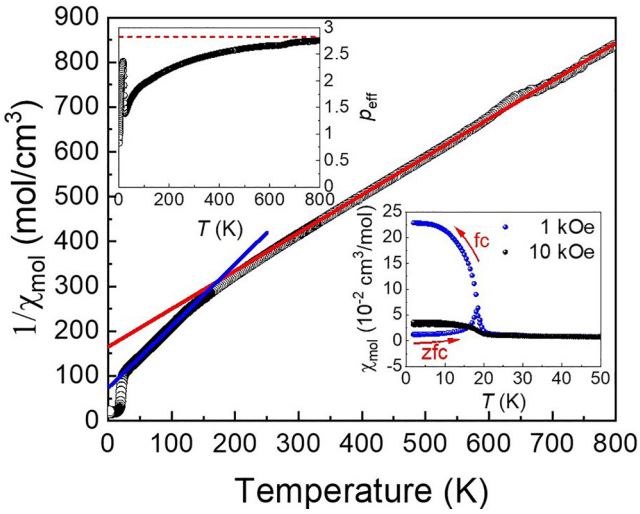


FIG. 2. Magnetic susceptibility of a polycrystalline sample of VF_3 measured in external magnetic fields of 1 and 10 kOe. The upper inset displays the effective magnetic moment calculated according to Eq. (2). The horizontal dashed line indicates a value of $g\sqrt{S(S+1)}$, with $S = 1$ and $g = 2$. The lower inset shows the low-temperature regime, highlighting the hysteresis of the field-cooled (fc) and the zero-field-cooled (zfc) susceptibilities below ∼19 K, which is clearly seen for 1 kOe. The hysteresis is largely suppressed by a magnetic field of 10 kOe.

and

$$\theta = -54(1)\ \text{K}.$$

The kink at ∼120 K in the inverse susceptibility cannot be attributed to the magnetic behavior of the V_2O_3 impurity identified by x-ray powder diffraction (XRPD) (see Fig. 8 below). V_2O_3 undergoes a Mott transition to an insulating antiferromagnetic (AFM) phase at ∼155 K with a decrease of the magnetic susceptibility, viz., an increase in the inverse susceptibility [17,18]. The reduction of the effective magnetic moment at ∼120 K, as also observed by Gossard *et al.* [13], must instead be attributed to an electronic effect leading to a reduction of the spin moment. It is associated with the structural phase transition at ∼120 K that will be described in detail below.

As also already observed by Gossard *et al.*, our magnetic susceptibility exhibits a stark upturn below ∼19 K due to spin canting leading to a weak ferromagnetic moment of $0.19\mu_B$ [13]. As is typically observed for a weak ferromagnet, the field-cooled magnetic susceptibility collected with an external field of 1 kOe shows a ferromagnetlike increase which can be readily suppressed by raising the magnetic field to 10 kOe (see inset of Fig. 2).

The heat capacity of our VF_3 sample is displayed in Fig. 3. Our data are essentially identical to those published earlier by Gossard *et al.* [13]. The anomaly near ∼120 K linked to the structural PT is clearly resolved and centered at ∼115 K, somewhat lower that the observation by Gossard and collaborators. The low-temperature λ-type anomaly associated with the magnetic PT is rather sharp and peaks at 18.8(1) K. The entropy contained in the magnetic anomaly amounts to $0.79R$, consistent with the findings by Gossard *et al.*

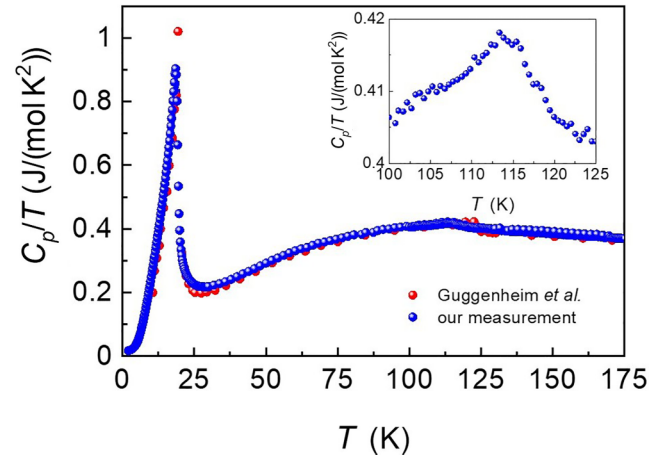


FIG. 3. Specific heat capacity of a polycrystalline sample of VF_3 (blue dots) in comparison to the results reported earlier by Gossard *et al.* [13] (red dots). The inset displays the temperature region at around 115 K.

B. Electron paramagnetic resonance

A typical EPR spectrum of our polycrystalline VF_3 sample collected at 275 K and at a microwave frequency of 9.48 GHz is displayed in Fig. 4. The powder spectrum is rather broad and characteristic of an EPR spectrum of a polycrystalline sample comprising magnetic entities [19]. It can be very well modeled by superposing the field derivatives of three Lorentzian-shaped resonance lines while also taking into account $\pm\omega$ resonances according to

$$\frac{dP_{\text{abs}}}{dH} \propto \sum_{i=1}^{3} \frac{d}{dH}\left(\frac{\Delta H_i + \alpha(H - H_{\text{res,i}})}{(H - H_{\text{res,i}})^2 + \Delta H_i^2} + \frac{\Delta H_i + \alpha(H + H_{\text{res,i}})}{(H + H_{\text{res,i}})^2 + \Delta H_i^2}\right). \quad (3)$$

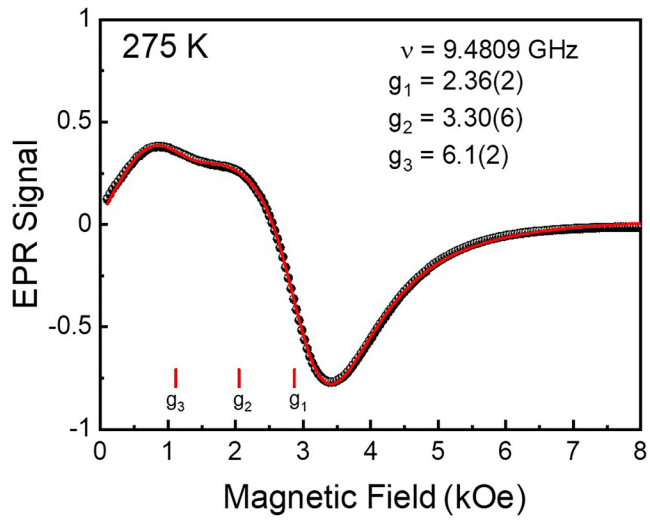


FIG. 4. Electron paramagnetic resonance spectrum of VF_3 (black dots) taken at 275 K with a microwave frequency of 9.4809 GHz. Fit of the spectrum (solid red line) by superposing three Lorentzian resonance lines according to Eq. (3). The resulting g factors for the three resonance lines are listed in the legend.

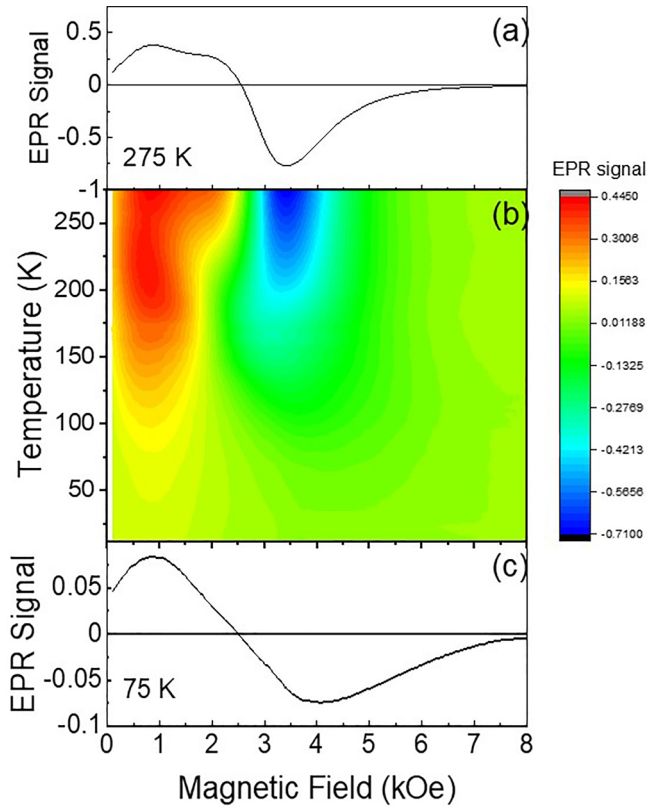


FIG. 5. Electron paramagnetic resonance spectra of VF_3 collected with a microwave frequency of 9.4809 GHz. (a) and (c) Spectra at 275 and 75 K. (b) Contour plot of a series of EPR spectra between room temperature and 10 K, highlighting the impact of the structural PT at ∼118 K on the magnetic properties.

P_{abs} is the absorbed microwave power, ΔH_i are the half widths at half maxima, H_i $(i = 1, \ldots, 3)$ are the resonance fields, and α measures the degree of admixture of dispersion to the signal. However, the addition of dispersion turns out not to be necessary (i.e., $\alpha = 0$), as may be expected for an insulating system. Additionally, a small background offset is also taken into account.

The EPR spectrum broadens with decreasing temperature and collapses to a single line at low temperatures. A clear drop in the EPR intensity takes place at ∼110 K (see Fig. 5), paralleling the PT seen in the magnetic susceptibility and the heat capacity.

IV. CRYSTAL STRUCTURE

At room temperature VF_3 crystallizes in the trigonal crystal system (space group R-3c, No. 167) with V and F atoms at Wyckoff sites 6b and 18e. The crystal structure, first determined by Jack and Gutmann [1], features regular VF_6 octahedra interconnected via common F atoms. The six V-F distances amount to 1.930 Å; the shortest V-V distances amount to 3.709 Å [1]. Figure 6 displays the room-temperature SPD pattern of our VF_3 sample collected with synchrotron radiation with a wavelength of 0.35421 Å together with a Rietveld profile refinement of the pattern. In addition to the Bragg reflections of VF_3, we observe several extra reflections, most of which originate from a V_2O_3

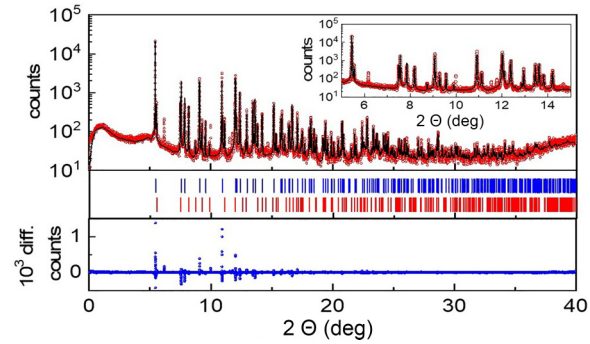


FIG. 6. Synchrotron powder diffraction pattern of our sample of VF_3 collected at room temperature (x-ray wavelength of 0.35421 Å). The top panel displays the data (red dots) and the result of the Rietveld profile refinement (solid black line). The vertical bars in the middle panel indicate the Bragg angles of the reflections used to calculate the refined pattern. Blue and red vertical bars refer to VF_3 and V_2O_3, respectively. The solid blue line in the bottom panel displays the difference between measured and calculated counts. The inset shows the refined pattern on an enlarged scale.

impurity (∼10 wt %) [20]. Some very sharp reflections were checked against binary V-F phases (VF_2, VF_4, VF_5) and ternary V-F-O and quaternary V-F-H-O phases. However, we were not able to attribute these extra reflections to one of these known phases [21]. We note that these sharp extra reflections are not present in the patterns collected with the cryostat below 22 K. Table I summarizes the lattice parameters and the atom coordinates of the room temperature crystal structure of VF_3 in comparison with the results reported earlier by Daniel *et al.* [4]. Below ∼120 K Bragg reflections with indices $-hkl = 3n$ split (see, e.g., Fig. 7), indicating a symmetry reduction concerning the F atoms occupying Wyckoff position 18e in space group $R\bar{3}c$. Figure 7 shows a contour plot highlighting the splitting of some (214, 300) Bragg reflections below ∼120 K.

The diffraction pattern collected at 80 K could be indexed on the basis of a monoclinic unit cell. A successful profile

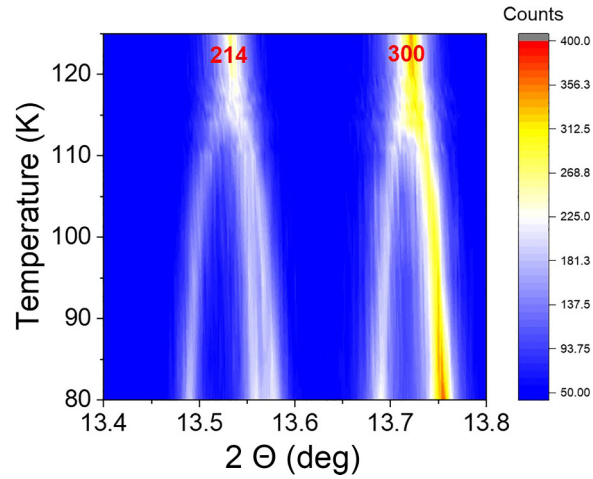


FIG. 7. Contour plot of a section of the SPD patterns between 125 and 80 K, highlighting the splitting of the (214) and (300) Bragg reflections below ∼120 K.

TABLE I. Lattice parameters, atom positions, displacement parameters, B, and cell volume of VF_3 at room temperature (RT) and at the indicated temperatures obtained from the synchrotron powder diffraction pattern collected with ESRF's powder diffractometer ID31.

T (K)	RT	RT	120	80
Space group	$R\bar{3}c$ [4]	$R\bar{3}c$	$R\bar{3}c$	$C2/c$
a (Å)	5.168(2)	5.17288(3)	5.13711(5)	9.42119(5)
b (Å)	5.168(2)	5.17288(3)	5.13711(5)	5.11804(3)
c (Å)	13.438(5)	13.4161(1)	13.4263(2)	13.43108(8)
γ/β (deg)	120	120	120	161.6025(1)
Volume (Å^3)	310.8(2)	310.900(4)	306.848(5)	204.394(2)
V				
Wyckoff site	6*b*	6*b*	6*b*	4*a*
x	0	0	0	0
y	0	0	0	0
z	0	0	0	0
B (Å^2)		0.38(1)	0.33(3)	0.34(1)
F1				
Wyckoff site	18*e*	18*e*	18*e*	4*e*
x	0.40001(3)	0.4040(1)	0.4026(3)	0
y	0	0	0	0.3960(3)
z	1/4	1/4	1/4	1/4
B (Å^2)		0.74(3)	0.43(5)	0.29(4)
F2				
Wyckoff site				8*f*
x				0.5925(4)
y				0.7986(3)
z				0.6444(3)
B (Å^2)				0.41(2)
R_P (%)		4.75	4.96	4.09
R_f (%)		4.15	4.06	5.98

refinement (see, e.g., Fig. 8, top panel) was achieved assuming space group $C2/c$ (No. 15). Figure 8 displays the Rietveld profile refinement of the 80 K SPD pattern. Figure 9 displays a sketch of the unit cell in space group $C2/c$ in comparison to the unit cell in space group R-3c (see the Supplemental Material for the standard setting of the low-temperature $C2/c$ crystal structure [22]). Figures 10 and 11 show the tempera-

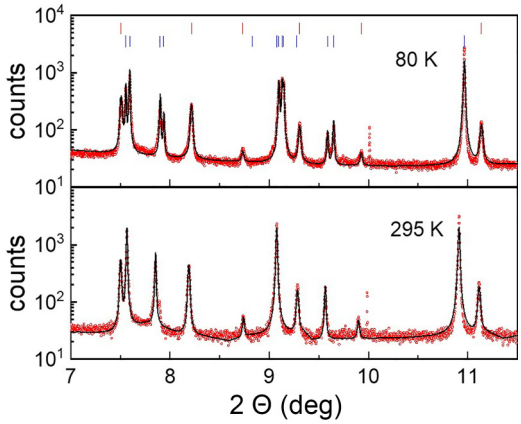


FIG. 8. Comparison of the synchrotron powder diffraction patterns of our sample of VF_3 collected at room temperature and at 80 K (X-ray wavelength 0.35421 Å). In the upper panel red and blue vertical bars denote the Bragg angles of VF_3 and V_2O_3, respectively, used to calculate the refined pattern shown by the solid black line.

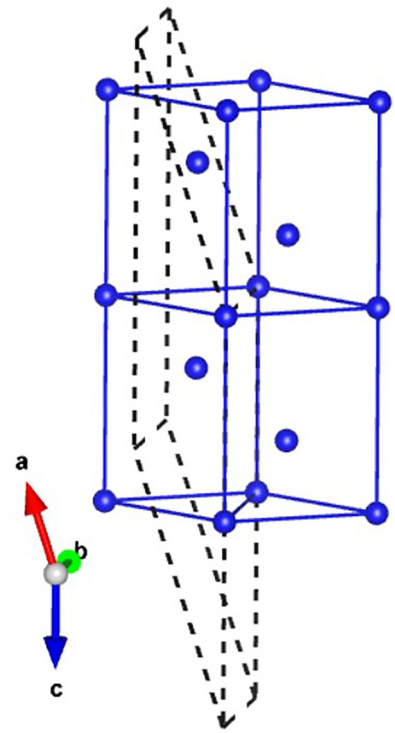


FIG. 9. Comparison of the unit cells in space groups $R\bar{3}c$ (solid blue lines) and $C2/c$ (dashed black lines). Only V atoms are shown by the blue spheres.

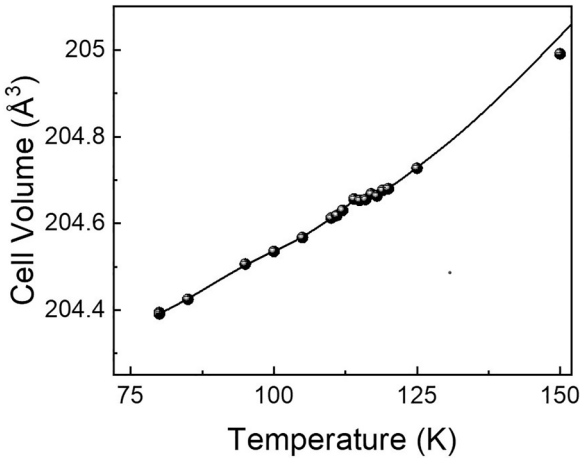


FIG. 10. Cell volume of VF_3 as derived from Rietveld profile refinements of the SPD patterns collected with ESRF's diffractometer ID31 (x-ray wavelength of 0.35421 Å) assuming space group $C2/c$.

ture dependence of the cell volume and the lattice parameters of VF_3. Tables I and II summarize the lattice parameters and relevant interatomic distances of the crystal structure of VF_3 at room temperature and at 80 K, respectively. The structural PT to monoclinic symmetry is seen as a faint anomaly in the cell volume but more clearly in the lattice parameters. Whereas lattice parameters a and b and the monoclinic angle β contract

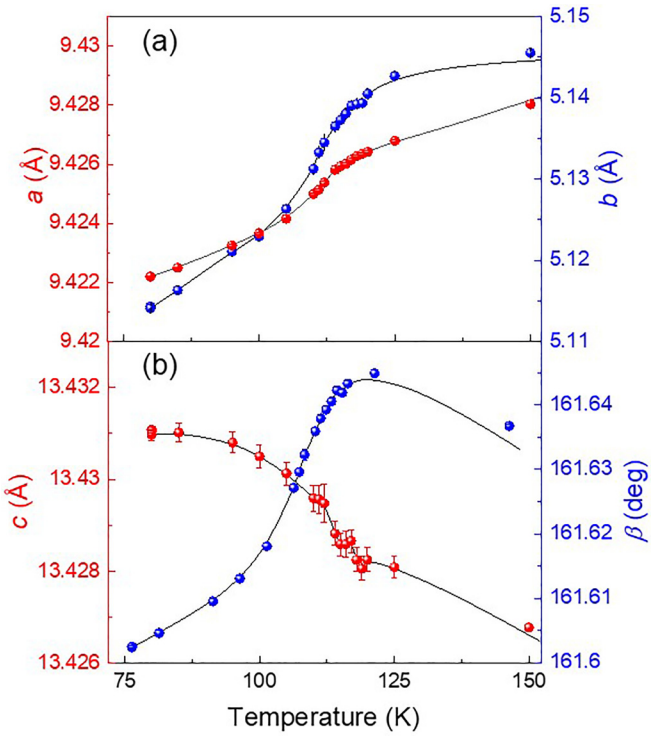


FIG. 11. Lattice parameters of VF_3 as a function of temperature as determined from Rietveld profile refinements of the synchrotron powder diffraction patterns. The solid lines are guides to the eye. The two patterns collected at temperatures above the structural phase transition have also been refined assuming monoclinic space group $C2/c$.

TABLE II. Interatomic V-V and V-F nearest-neighbor distances calculated from the structural parameters listed in Table I.

T (K)	RT	300	120	80
Space group	R-3c [4]	$R\bar{3}c$	$R\bar{3}c$	$C2/c$
V-V (Å)	5.168(2)	5.1728(1)	5.1378(1)	5.11802(5)
V-V (Å)				5.1421(4)
V-V (Å)				5.1421(4)
V-F1 (Å)	1.9355(8)	1.9304(6)	1.9239(8)	1.9314(4)
V-F2 (Å)				1.910(3)
V-F2 (Å)				1.953(3)
F1-F1 (Å)	2.7257(5)	2.7257(5)	2.7109(4)	
F1-F1 (Å)	2.7342(5)	2.7343(5)	2.731(1)	
F1-F2 (Å)				2.711(2)
F1-F2 (Å)				2.722(5)
F1-F2 (Å)				2.744(1)
F1-F2 (Å)				2.750(5)

below the PT, c expands by about 200 ppm between 120 and 80 K. The largest relative contraction is seen for b. It amounts to 0.6% (see also Fig. 11). The symmetry reduction at the structural PT involves a small orthorhombic distortion of the V-F octahedra with a slight differentiation of the V-F distances (for details see Table II).

Table I summarizes characteristic structural parameters for VF_3 in the high-temperature $R\bar{3}c$ phase and below the structural phase transition obtained from Rietveld profile refinements of the synchrotron powder diffraction patterns collected with ESRF's diffractometer ID31.

A. Neutron powder diffraction

1. Magnetic structure

Neutron powder diffraction patterns collected on ILL's medium-resolution high-intensity diffractometer D20 below ∼18 K revealed two clearly resolved additional Bragg reflections at 31.2° (d = 4.51 Å) and 33.1° (d = 4.26 Å; see Fig. 12). The intensities of these reflections increase with decreasing temperature and saturate below about 10 K (see the inset of Fig. 12).

The two magnetic Bragg reflections can be indexed based on the propagation vector $\vec{k}$ = (0, 0, 1) as (−2, 0, 3) and as (0, 0, 1)/(1, 1, −3), with the latter two reflections overlapping. Using the propagation vector in the subroutine BasIreps implemented in the fullprof software results in two one-dimensional irreducible representations, each contained three times in Γ_k with three real basis functions. A satisfactory refinement can be achieved with a magnetic structure model aligning the V moments of $\sim 1\mu_B$ along b of the monoclinic unit cell, i.e., within the trigonal layers of the high-temperature trigonal crystal structure. The refinement also reveals that magnetic Bragg reflections at higher Bragg angles are considerably weaker in intensity and partly overlap with nuclear reflections.

In the magnetic structure of VF_3 each V triangular layer is ferromagnetically aligned, and successive layers point in the opposite direction. Overall, the magnetic structure of VF_3 can be understood as an antiferromagnetic sequence of ferromagnetic layers (magnetic point group $2'/m'$; see

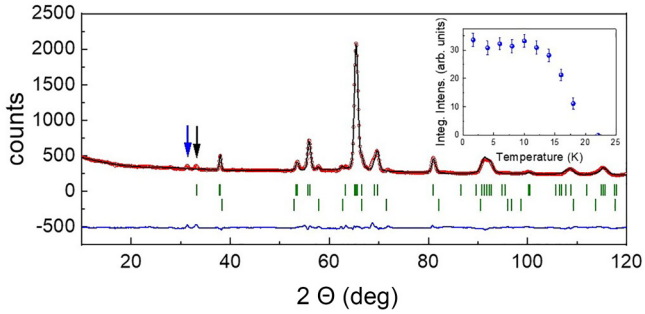


FIG. 12. Neutron powder diffraction patterns (red dots) collected on ILL's medium-resolution high-intensity two-axis diffractometer D20 at 1.65 K together with a Rietveld profile refinement (solid black line) assuming the nuclear contributions of VF_3 and V_2O_3 ($R_{\text{Bragg}} = 3.71$, $R_f = 3.09$, $\chi^2 = 0.21$). The green vertical bars mark the Bragg angles of the reflections of VF_3 and V_2O_3 used to calculate the refined pattern. The solid blue line below displays the difference between measured and calculated patterns. The two prominent magnetic Bragg peaks at $d = 4.26$ Å and $d = 4.51$ Å are marked by vertical arrows. The inset shows the integrated intensity of the magnetic Bragg reflection at $d = 4.51$ Å.

Fig. 13). The magnetic structure of VF_3 (Fig. 14) thus bears close similarity to that of FeF_3; however, due to the decay to monoclinic symmetry the direction of the moment vectors is now fixed, whereas for FeF_3 the direction of the spins on the *ab* plane remains undetermined (see the MAGNDATA collection in the Bilbao Crystallographic Server) [23,24]. Given that only two clear magnetic reflections are well resolved in the neutron powder diffraction pattern, our magnetic structure solution was not able to capture a weak ferromagnetic moment, which, however, is permitted by the irreducible representations.

Figure 15 shows the refined magnetic moment of the V atoms as a function of temperature. The moments exhibit a sharp increase below 18.4(2) K, pass through a very

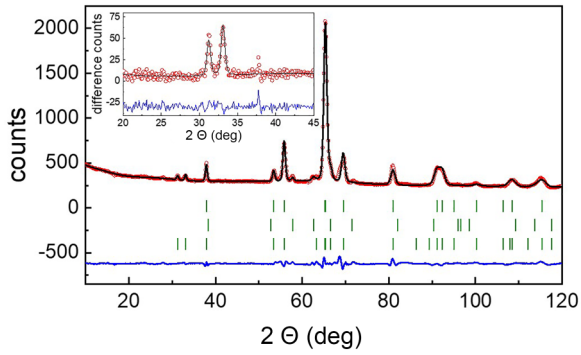


FIG. 13. Neutron powder diffraction patterns at 1.65 K compared to the Rietveld profile refinement assuming three phases, namely, VF_3, the V_2O_3 nuclear phase, and the magnetic phase of VF_3 with the propagation vector $\vec{\tau} = (0,0,1)$. The red dots show the measured pattern, the solid black line represents the profile refinement, and the blue solid line at the bottom highlights the difference between measured and calculated patterns. The inset highlights the two prominent magnetic Bragg reflections (difference pattern 1.65–22 K) together with the profile refinement.

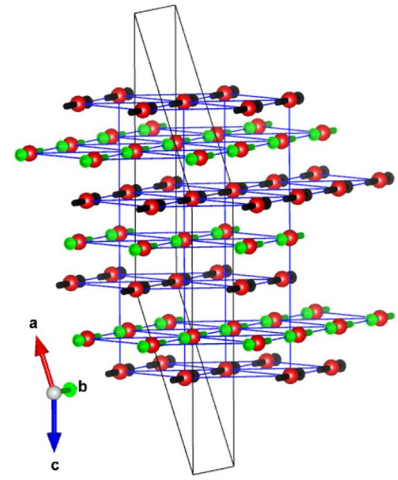


FIG. 14. Magnetic structure of VF_3 at 1.65 K. The thin gray lines highlight a nuclear unit cell in monoclinic space group $C2/c$. The blue solid lines connect V atoms in the triangular layers. The moments are parallel to monoclinic *b* and amount to $\sim 1\mu_B$. Black and green vectors refer to V atoms at (0, 0, 0/1/2, 1/2 0) and (0, 0, 1/2/1/2, 1/2, 1/2) and equivalent positions, respectively.

shallow maximum at ∼8 K, and saturate at a value of $1.02(5)\mu_B$ for $T \to 0$ K. The stark increase below 18.4 K is rather reminiscent of a first-order phase transition. This finding is supported by the small critical exponent obtained by fitting the temperature dependence of the ordered moments, which is incompatible with standard universality classes (see Fig. 15). As discussed below, the moment increase below the magnetic phase transition goes along with some magnetostriction effects best seen in the *b* lattice parameter and the temperature dependence of the cell volume below T_C.

2. Spontaneous magnetostriction

From the sets of NPD and SPD patterns collected at stabilized temperature below 22 K with ILL's medium-resolution

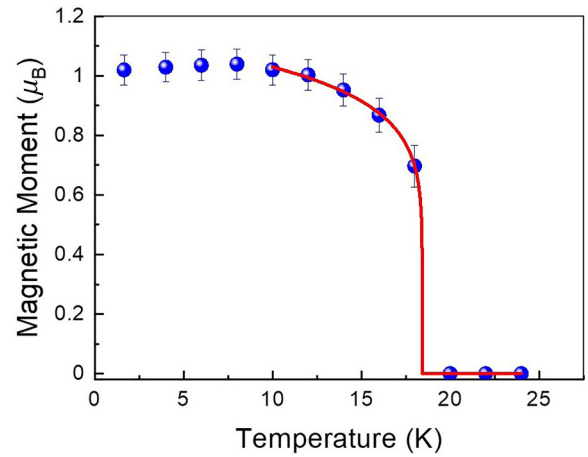


FIG. 15. Temperature dependence of the magnetic moment of the V atoms in VF_3. The solid red line represents a critical power law according to $I \propto t^{\beta}$, with $t = (T - T_C)/T_C$, $T_C = 18.4(2)$ K, and critical exponent $\beta = 0.13(1)$.

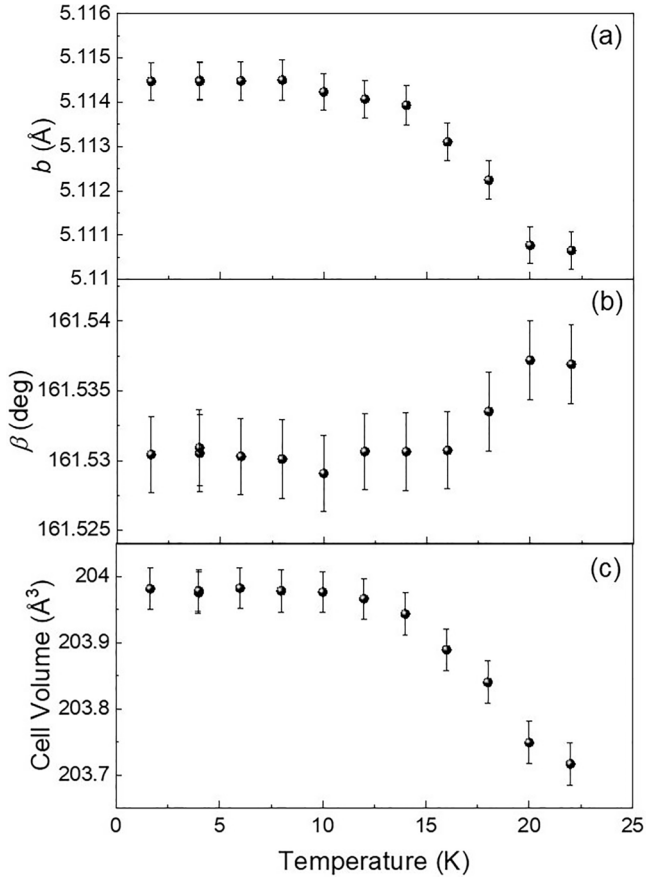


FIG. 16. (a) Lattice parameter b, (b) monoclinic angle β, and (c) cell volume V_{cell} as a function of temperature as obtained from Rietveld profile refinements of the NPD patterns collected with ILL's medium-resolution high-intensity two-axis diffractometer D20 below 22 K.

high-intensity diffractometer D20 and ESRF's beamline ID31 the low-temperature crystal structure could be refined. In the case of the NPD pattern refinement the atom positional parameters were kept constant at the values obtained from refinement of the SPD pattern collected at 80 K.

Figure 16 displays the lattice parameters as a function of temperature below 22 K. V magnetic moment AFM ordering below ∼18 K causes a small, but noticeable, magnetostrictive expansion of the cell volume and the b lattice parameter (Fig. 16), whereas the lattice parameters a (<80 ppm) and c (<70 ppm; not shown) remain approximately constant between 22 and 1.65 K. The unit cell volume increases by $\Delta V/V(20\ \text{K}) \approx 0.1\%$, and the monoclinic angle β decreases by ∼25 ppm between 22 and 1.65 K. As shown in detail in the Supplemental Material [21], Rietveld profile refinements of a set of SPD patterns collected below 22 K revealed analogous progress of the lattice parameters and the unit cell volume with temperature below T_C [22].

V. DISCUSSION AND CONCLUSIONS

Unlike most other 3d transition metal trifluorides like MF_3 (M = Ti, Cr, Fe, Co), VF_3 exhibits a structural PT at ∼120 K with a symmetry reduction from $R\bar{3}c$ to a monoclinic low-temperature structure best described in space group $C2/c$. An analogous symmetry reduction was reported for MnF_3 by Hepworth *et al.* and more recently confirmed by Hunter *et al.* and Bandemehr *et al.* [5,6,11]. However, in contrast to VF_3 the structural phase transition in MnF_3 appears already above room temperature. Together with MnF_3, VF_3 thus constitutes an exception to the MF_3 series. Our magnetic susceptibility and heat capacity data confirm the structural PT of VF_3 conjectured before by Gossard *et al.* [13]. By using temperature-dependent SPD data we determined the parameters of the low-temperature crystal structure. The structural PT leads to a distortion of the trigonal cell and a minute orthorhombic distortion of the F coordination shell of the V atoms. The crystal structure of VF_3 at low temperatures thus bears close similarities to the crystal structure of MnF_3, which exhibits the monoclinic distortion already at room temperature, with a more pronounced distortion of the F octahedron coordination shell of the Mn^{3+} cations (see Supplemental Material for more details [22]). The structural PT leads to a modification of the magnetic properties, as is seen, e.g., in the temperature-dependent electron paramagnetic resonance spectra. Also, the magnetic susceptibility undergoes a change from the high-temperature Curie-Weiss behavior consistent with a spin-only value of $S = 1$. The magnetic susceptibility data indicate weak ferromagnetism below ∼19 K, similar to the findings for CoF_3 and FeF_3. Neutron powder diffraction data reveal that the appearance of weak ferromagnetism is connected to a transition to an A-type antiferromagnetic structure described in magnetic space group $C2'/c'$. The Néel temperature of VF_3 is, by a factor of 3, smaller than the paramagnetic Curie-Weiss temperature and, remarkably, is more than an order of magnitude lower than the Néel temperatures of FeF_3 and CoF_3. The ordered magnetic moment refined from the neutron powder diffraction data at 1.65 K amounts to $\approx 1\mu_B$, which is a factor of 2 smaller than the spin-only value expected for the free V^{3+} spin $S = 1$ cation. Each ferromagnetic aligned V triangular layer is connected to adjacent antiferromagnetically aligned V layers (V-V distance ≈ 3.71 Å) via common F^- anions (V-F-V bonding angle ≈148°) supporting AFM superexchange [25].

The structural phase transition induces a differentiation of the V-F distances from the V atoms to the F atoms in the octahedral coordination shells and also to a minute differentiation (∼0.16°) of the V-F-V bonding angles, which is, however, significantly smaller than that found for MnF_3 [6]. For a compilation of typical M-F-M bonding angles in other MF_3 phases, see, e.g., Ref. [26].

Figure 17 highlights a VF_6 octahedron. The F octahedra are elongated and, within the equatorial plane, slightly orthorhombically distorted. In a one-electron picture this leads to a lifting of the threefold orbital degeneracy of the t_{2g} orbitals and to orbital ordering.

The decrease in the effective magnetic moment below ∼120 K and the unexpectedly small ordered magnetic moment of $1\mu_B$ found from the neutron diffraction experiments are interesting. Hund's rules give a ^3F term as the ground term for a d^2 electron configuration. Taking the interelectron repulsion between d electrons into account, there are several excited terms (total degeneracy of 45) [27,28]; among them, the first one with the same spin multiplicity is ^3P at 15B. Here,

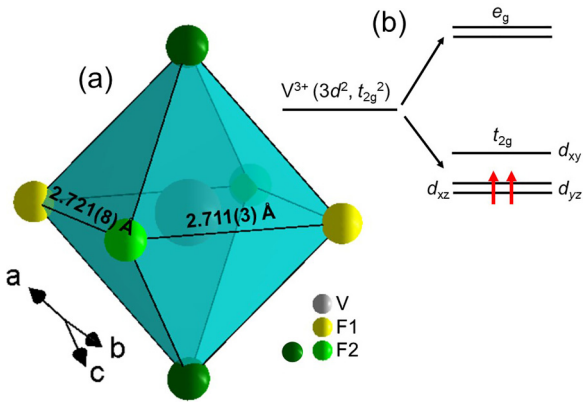


FIG. 17. (a) Fluorine octahedral coordination of the V atoms in the low-temperature crystal structure. For characteristic V-F distances, see Table II. The F octahedra are elongated (V-F2 distance: 1.953 Å). The V-F distances in the equatorial plane (1.931 and 1.910 Å) differ by 1.1%. Equatorial F1-F2 distances are indicated. (b) Schematic one-electron orbital energy level scheme for a V^{3+} cation in the elongated F octahedral coordination.

B is the second Racah parameter, which for V^{3+} amounts to $\sim$860 cm^{-1}[28]. An octahedral crystal electric field acting on the terms ^3F and ^3P brings about $^3T_1(F, P)$ terms. Depending on the magnitude of the crystal electric field ^3F and ^3P can mix, with the consequence that the wave functions and the magnetic properties of a d^2 electron system depend on the strength of the crystal electric field. In addition, spin-orbit coupling splits the $^3T_1(F)$ ground term into a quintuplet with a g factor depending on the mixing of the ^3F and ^3P wave functions, viz., the magnitude of the crystal electric field. As a consequence, the effective magnetic moment p_{eff} entering, e.g., into the Curie-Weiss law becomes largely temperature dependent on the crystal field and the spin-orbit coupling, both being subject to nephelauxetic effects [29,30]. Along with antiferromagnetic ordering, the unit cell of VF_3 expands (see Fig. 16), and the fluorine coordination of the V atoms becomes less compressed (see Table III). The cell expansion will reduce the splitting of the t_{2g} orbitals and also alter the spin-orbit coupling.

While at room temperature the effective magnetic moment is typically close to 2.8μ_B, consistent with a spin-only value of spin $S = 1$ and a g factor of $\sim$2, largely independent of the magnitude of the crystal electric field, the effective moment falls off rather rapidly towards low temperatures with larger differences between weak and strong crystal fields [28]. This prediction is consistent with our magnetic susceptibility data and also with the reduced magnetic moment refined from the neutron powder diffraction data.

TABLE III. V-F nearest-neighbor distances at 22 and 5 K in the paramagnetic and antiferromagnetic states.

	22 K	5 K
V-F1 (Å)	1.9302(18)	1.9302(8)
V-F2 (Å)	1.889(11)	1.904(5)
V-F2 (Å)	1.958(10)	1.960(3)

VF_3 exhibits noticeable spontaneous negative thermal expansion of the cell volume and the b axis starting at T_N. For MnF_3 similar spontaneous negative thermal expansion has been reported [11,31]. Whereas in MnF_3 (with $T_N \approx 43$ K) all lattice parameters expand below T_N, in VF_3 c and the monoclinic angle β contract, and a exhibits only a minor response to magnetic long-range ordering.

In summary, we have conclusively determined the low-temperature crystal and magnetic structures of VF_3 and detected spontaneous magnetostriction. Deviations from the spin-only magnetism of V^{3+} in VF_3 are ascribed to orbital ordering effects.

ACKNOWLEDGMENTS

Useful discussions with P. Puphal are gratefully acknowledged. Expert experimental assistance from E. Brücher is gratefully acknowledged.

DATA AVAILABILITY

The data that support the findings of this article are not publicly available. The data are available from the authors upon reasonable request.

[1] K. H. Jack and V. Gutmann, The crystal structure of vanadium trifluoride VF_3, Acta Crystallogr. **4**, 246 (1951).
[2] M. A. Hepworth, K. H. Jack, R. D. Peacock, and G. J. Westland, The crystal structures of the trifluorides of iron, cobalt, ruthenium, rhodium, palladium and iridium, Acta Crystallogr. **10**, 63 (1957).
[3] K. Knox, Structures of chromium(iii) fluoride, Acta Crystallogr. **13**, 507 (1960).
[4] P. Daniel, A. Bulou, M. Leblanc, M. Rousseau, and J. Nouet, Structural and vibrational study of VF_3, Mater. Res. Bull. **25**, 413 (1990).
[5] M. A. Hepworth and K. H. Jack, The crystal structure of manganese trifluoride, MnF_3, Acta Crystallogr. **10**, 345 (1957).
[6] J. Bandemehr, C. Stoll, G. Heymann, S. I. Ivlev, A. J. Karttunen, M. Conrad, H. Huppertz, and F. Kraus, The crystal structure of MnF_3 revisited, Z. Anorg. Allg. Chem. **646**, 882 (2020).
[7] E. O. Wollan, H. R. Child, W. C. Koehler, and M. K. Wilkinson, Antiferromagnetic properties of the iron group trifluorides, Phys. Rev. **112**, 1132 (1958).
[8] U. Bertelsen, J. M. Knudsen, and H. Krogh, Mössbauer effect in FeF_3, Phys. Status Solidi B **22**, 59 (1967).

[9] R. Bozorth and J. Nielsen, Antiferromagnetism of $CuF_2 \cdot 2H_2O$ and MnF_3, Phys. Rev. **110**, 879 (1958).
[10] R. Bozorth and V. Kramer, Some ferrimagnetic and antiferromagnetic materials at low temperatures, J. Phys. Radium **20**, 393 (1959).
[11] B. A. Hunter, B. J. Kennedy, and T. Vogt, Magnetostriction in a simple trivalent manganese perovskite, Phys. Rev. B **69**, 020410(R) (2004).
[12] S. Lee, S. Torii, Y. Ishikawa, M. Yonemura, T. Moyoshi, and T. Kamiyama, Weak-ferromagnetism of CoF_3 and FeF_3, Physica B (Amsterdam, Neth.) **551**, 94 (2018).
[13] A. C. Gossard, H. J. Guggenheim, F. S. L. Hsu, and R. C. Sherwood, Magnetic ordering of VF_3, AIP Conf. Proc. **5**, 302 (1972).
[14] T. C. Hansen, P. F. Henry, H. E. Fischer, J. Torregrossa, and P. Convert, The D20 instrument at the ILL: A versatile high-intensity two-axis neutron diffractometer, Meas. Sci. Technol. **19**, 034001 (2008).
[15] J. Rodríguez-Carvajal, Recent advances in magnetic structure determination by neutron powder diffraction, Physica B (Amsterdam, Neth.) **192**, 55 (1993).
[16] G. A. Bain and J. F. Berry, Diamagnetic corrections and Pascal's constants, J. Chem. Educ. **85**, 532 (2008).
[17] K. Kosuge, The phase diagram and phase transition of the $V_2O_3-V_2O_5$ system, J. Phys. Chem. Solids **28**, 1613 (1967).
[18] P. D. Dernier and M. Marezio, Crystal structure of the low-temperature antiferromagnetic phase of V_2O_3, Phys. Rev. B **2**, 3771 (1970).
[19] J. A. Weil, J. R. Bolton, and J. E. Wertz, *Electron Paramagnetic Resonance: Elementary Theory and Practical Applications* (Wiley, New York, 1994).
[20] The amount of V_2O_3 impurity refers to the weight percent and was determined from x-ray diffraction patterns collected on a sample inserted into a 0.3 mm diameter capillary, which may result in a preferred selection and adulteration of the composition. The neutron diffraction measurements of the bulk sample indicated only about 5 wt % V_2O_3 impurity.
[21] Inorganic Crystal Structure Database (ICSD), FIZ Karlsruhe Leibniz Institute for Information Infrastructure, https://icsd.fiz-karlsruhe.de.
[22] See Supplemental Material at http://link.aps.org/supplemental/10.1103/3gzm-yxfb for the detailed results of the magnetic structure solution starting from monoclinic space group $C2/c$.
[23] S. V. Gallego, J. M. Perez-Mato, L. Elcoro, E. S. Tasci, R. M. Hanson, K. Momma, M. I. Aroyo, and G. Madariaga, *MAGNDATA*: Towards a database of magnetic structures. I. The commensurate case, J. Appl. Crystallogr. **49**, 1750 (2016).
[24] S. V. Gallego, J. M. Perez-Mato, L. Elcoro, E. S. Tasci, R. M. Hanson, M. I. Aroyo, and G. Madariaga, *MAGNDATA*: Towards a database of magnetic structures. II. The incommensurate case, J. Appl. Crystallogr. **49**, 1941 (2016).
[25] J. B. Goodenough, *Magnetism and the Chemical Bond* (Interscience, New York, 1963).
[26] U. Müller, *Symmetry Relationships between Crystal Structures* (Oxford University Press, Oxford, 2013).
[27] G. Racah, Theory of complex spectra. II, Phys. Rev. **62**, 438 (1942).
[28] F. E. Mabbs and D. J. Machin, *Magnetism and Transition Metal Complexes* (Chapman and Hall, London, 1973).
[29] E. König and S. Kremer, Complete theory of paramagnetism in transition metal ions IV. The d^2 and d^8 electron configurations in cubic (O_h and T_d), tetragonal (D_{4h}), and trigonal (D_{3d}) symmetry, Ber. Bunsenges. Phys. Chem. **79**, 192 (1975).
[30] H. Lueken, *Magnetochemie* (Teubner, Stuttgart, 1999).
[31] B. A. Hunter, T. Vogt, and B. J. Kennedy, Atomic and magnetic strutcure of MnF_3, Acta Crystallogr., Sect. A **58**, C146 (2002).